Backscattered Electrons

J. Goldstein et al., *Scanning Electron Microscopy and X-Ray Microanalysis*,
https://doi.org/10.1007/978-1-4939-6676-9_2

2

2.1 Origin

Close inspection of the trajectories in the Monte Carlo simulation of a flat, bulk target of copper at 0° tilt shown in Fig. 2.1 reveals that a significant fraction of the incident beam electrons undergo sufficient scattering events to completely reverse their initial direction of travel into the specimen, causing these electrons to return to the entrance surface and exit the specimen. These beam electrons that escape from the specimen are referred to as "backscattered electrons" (BSE) and constitute an important SEM imaging signal rich in information on specimen characteristics. The BSE signal can convey information on the specimen composition, topography, mass thickness, and crystallography. This module describes the properties of backscattered electrons and how those properties are modified by specimen characteristics to produce useful information in SEM images.

2.1.1 The Numerical Measure of Backscattered Electrons

Backscattered electrons are quantified with the "backscattered electron coefficient," η, defined as

$$\eta = N_{BSE} / N_B \quad (2.1)$$

where N_B is the number of beam electrons that enter the specimen and N_{BSE} is the number of those electrons that subsequently emerge as backscattered electrons.

2.2 Critical Properties of Backscattered Electrons

2.2.1 BSE Response to Specimen Composition (η vs. Atomic Number, Z)

Use the CASINO Monte Carlo simulation software, which reports η in the output, to examine the dependence of electron backscattering on the atomic number of the specimen.

Simulate at least 10,000 trajectories at an incident energy of $E_0 = 20$ keV and a surface tilt of 0° (i.e., the beam is perpendicular to the surface). Note that statistical variations will be observed in the calculation of η due to the different selections of the random numbers used in each simulation. Repetitions of this calculation will give a distribution of results, with a precision $p = (\eta\ N)^{1/2}/\eta\ N$, so that for $N = 10{,}000$ trajectories and $\eta \sim 0.15$ (Si), p is expected to be 2.5 %. Figure 2.2 shows the simulation of 500 trajectories in carbon, silicon, copper, and gold with an incident energy of $E_0 = 20$ keV and a surface tilt of 0°, showing qualitatively the increase in the number of backscattered electrons with atomic number.

Detailed experimental measurements of the backscattered electron coefficient as a function of the atomic number, Z, in highly polished, flat pure element targets confirm a generally monotonic increase in η with increasing Z, as shown in Fig. 2.3a, where the classic measurements made by Heinrich (1966) at a beam energy of 20 keV are plotted. The slope of η vs. Z is highest for low atomic number targets up to approximately $Z = 14$ (Si). As Z continues to increase into the range of

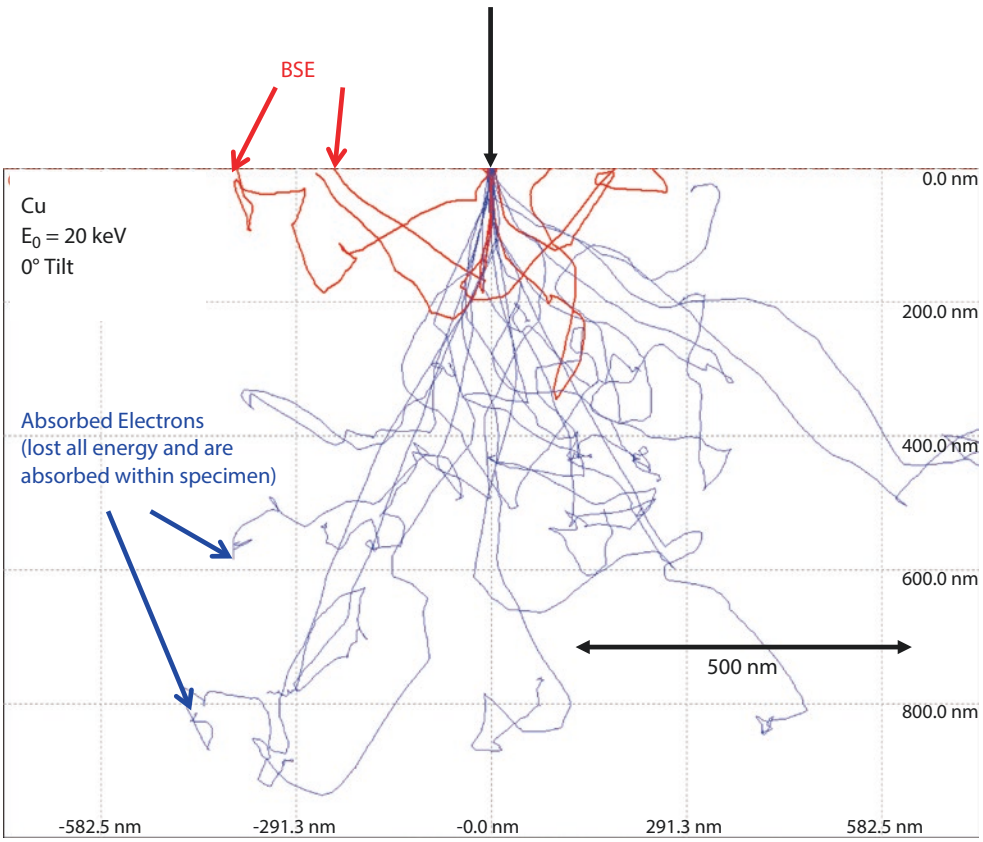

Fig. 2.1 Monte Carlo simulation of a flat, bulk target of copper at 0° tilt. Red trajectories lead to backscattering events

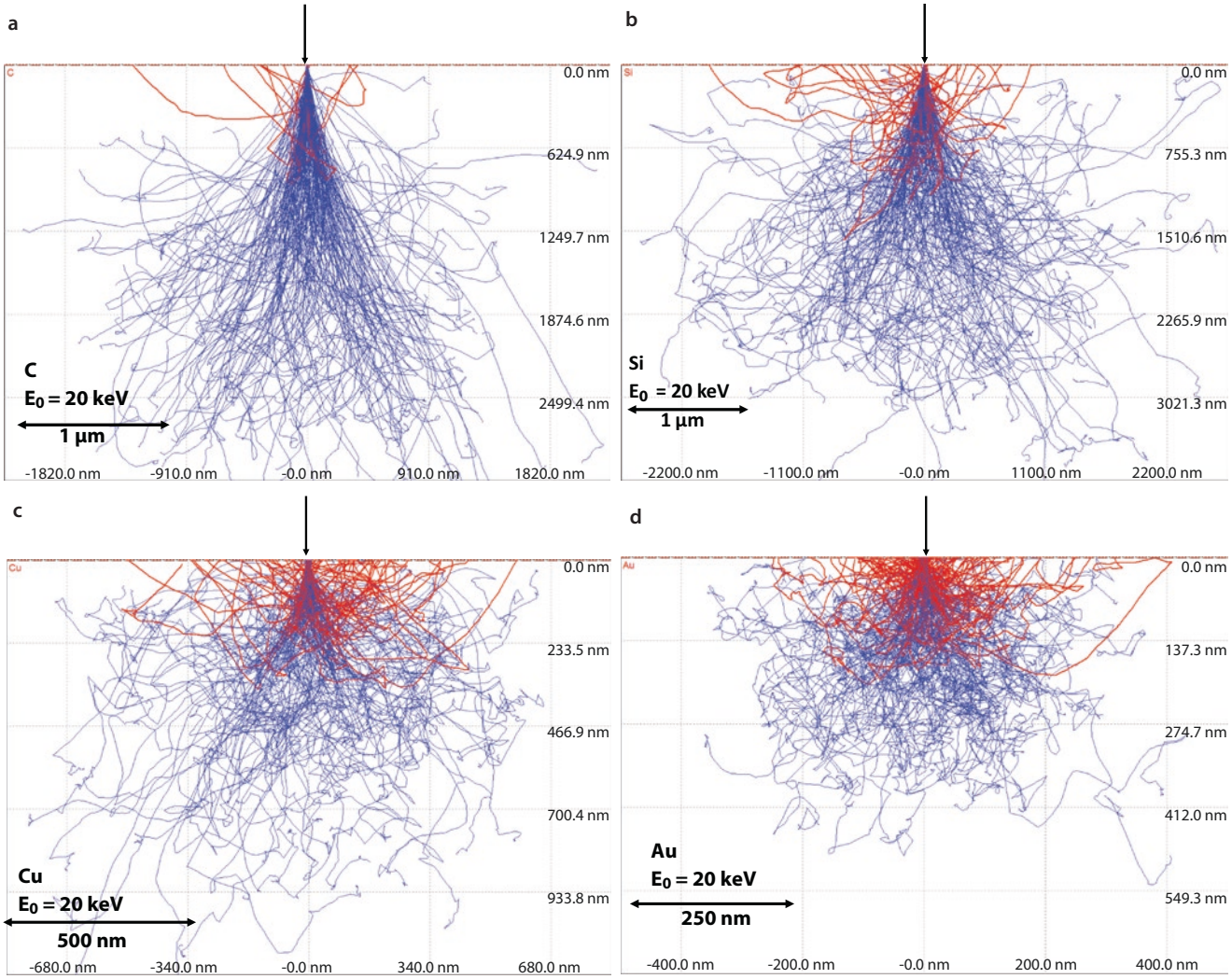

Fig. 2.2 **a** Monte Carlo simulation of 500 trajectories in carbon with an incident energy of $E_0 = 20$ keV and a surface tilt of 0° (CASINO Monte Carlo simulation). **b** Monte Carlo simulation of 500 trajectories in silicon with an incident energy of $E_0 = 20$ keV and a surface tilt of 0°. **c** Monte Carlo simulation of 500 trajectories in copper with an incident energy of $E_0 = 20$ keV and a surface tilt of 0°. **d** Monte Carlo simulation of 500 trajectories in gold with an incident energy of $E_0 = 20$ keV and a surface tilt of 0°. Red trajectories = backscattering

the transition elements, e.g., $Z = 26$ (Fe), the slope progressively decreases until at very high Z, e.g., the region around $Z = 79$ (Au), the slope becomes so shallow that there is very little change in η between adjacent elements. Plotted in addition to the experimental measurements in Fig. 2.3a is a mathematical fit to the 20 keV data developed by Reuter (1972):

$$\eta = -0.0254 + 0.016\,Z - 1.86\times10^{-4}\,Z^2 + 8.3\times10^{-7}\,Z^3 \qquad (2.2)$$

This fit provides a convenient estimate of η for those elements for which direct measurements do not exist.

Experimental measurements (Heinrich 1966) have shown that the backscattered electron coefficient of a mixture of atoms that is homogeneous on the atomic scale, such as a stoichiometric compound, a glass, or certain metallic alloys, can be accurately predicted from the mass concentrations of the elemental constituents and the values of η for those pure elements:

$$\eta_{\text{mixture}} = \Sigma \eta_i C_i \qquad (2.3)$$

where C is the mass (weight) fraction and i is an index that denotes all of the elements involved.

When measurements of η vs. Z are made at different beam energies, combining the experimental measurements of Heinrich and of Bishop in Fig. 2.3b, little dependence on the beam energy is found from 5 to 49 keV, with all of the measurements clustering relatively closely to the curve for the 20 keV data shown in Fig. 2.3a. This result is perhaps surprising in view of the strong dependence of the dimensions of the interaction volume on the incident beam energy. The weak dependence of η upon E_0 despite the strong dependence of the beam penetration upon E_0 can be understood as a near balance between the increased energy available at higher E_0, the lower rate of loss, dE/ds, with higher E_0, and the increased penetration. Thus, although a beam electron may penetrate more deeply at high E_0, it started with more

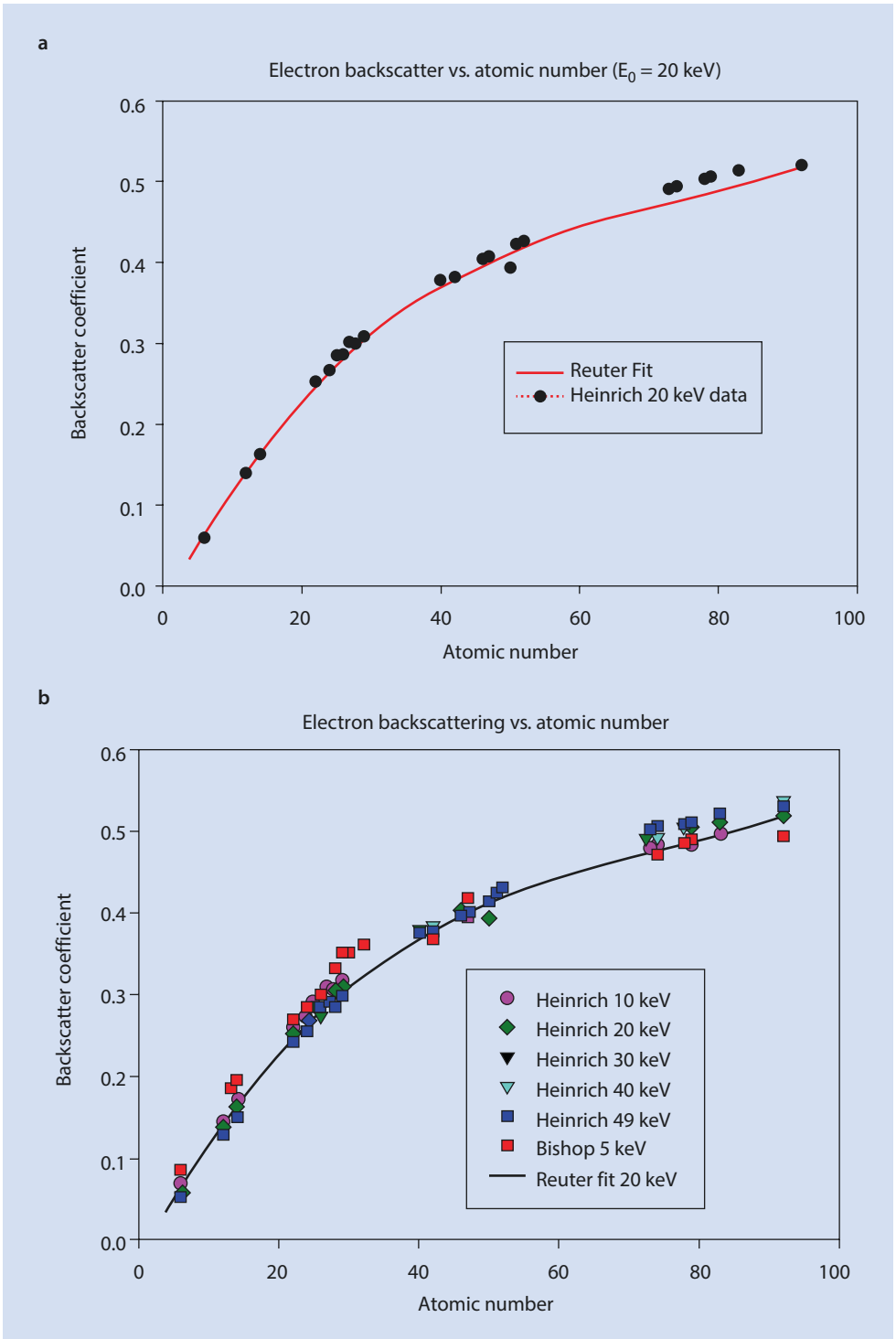

Fig. 2.3 **a** Electron backscatter coefficient as a function of atomic number for pure elements (Data of Heinrich 1966; fit of Reuter 1972). **b** Electron backscatter coefficient as a function of atomic number for pure elements for incident beam energies of 5 keV (data of Bishop 1966); 10 keV to 49 keV (Data of Heinrich 1966); Reuter's fit to Heinrich's 20 keV data, (1972))

energy and lost that energy at a lower initial rate than an electron at a lower incidence energy. Thus, a higher incidence energy electron, despite penetrating deeper in the specimen, retains more energy and can continue to scatter and progress through the target to escape.

SEM Image Contrast with BSE: "Atomic Number Contrast"

Whenever a signal that can be measured in the SEM, such as backscattered electrons, follows a predictable response to a specimen property of interest, such as composition, the physical basis for a "contrast mechanism" is established. Contrast, C_{tr}, is defined as

$$C_{tr} = (S_2 - S_1)/S_2 \text{ with } S_2 > S_1 \quad (2.4)$$

where S is the signal measured at any two locations of interest in the image field. As shown in Fig. 2.4, examples include the contrast between an object P_1 and the general background P_2 or between two objects that share an interface, P_3 and P_4. By this definition, contrast can range numerically from 0 to 1.

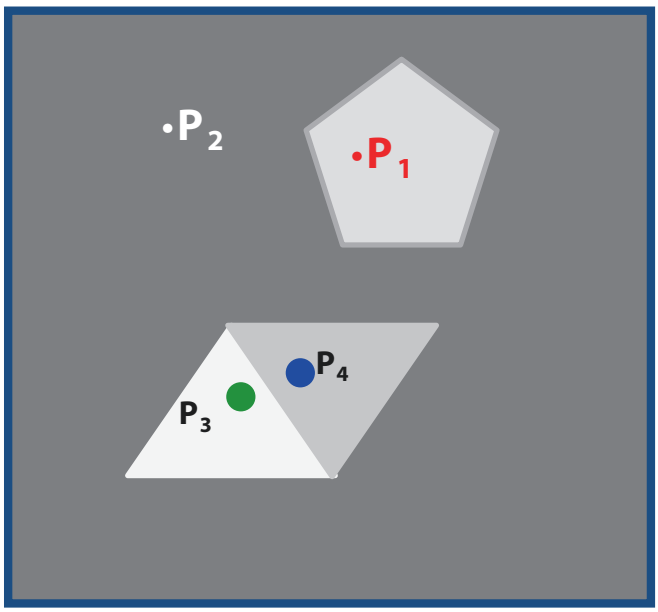

Fig. 2.4 Illustration of some possible contrast situations of interest, e.g., an object *P1* and the general background *P2* or between two objects that share an interface, *P3* and *P4*

The monotonic behavior of η vs. Z establishes the physical basis for "atomic number contrast" (also known as "Z-contrast" and "compositional contrast"). When an SEM BSE image is acquired from a flat specimen (i.e., no topography is present, at least on a scale no greater than about 5 % of the Kanaya–Okayama range for the particular material composition and incident beam energy), then local differences in composition can be observed as differences in the BSE intensity, which can be used to construct a meaningful gray-scale SEM image. The compositionally-different objects must have dimensions that are at least as large as the Kanaya-Okayama range for each distinct material so that a BSE signal characteristic of the particular composition can be measured over at least the center portion of the object. The BSE signal at beam locations on the edge of the object may be affected by penetration into the neighboring material(s).

From the definition of contrast, C_{tr}, atomic number contrast can be predicted between two materials with backscatter coefficients η_1 and η_2 when the measured signal S is proportional to η:

$$C_{tr} = (\eta_2 - \eta_1)/\eta_2 \text{ with } \eta_2 > \eta_1 \quad (2.5)$$

An example of atomic number contrast from a polished cross section of an aluminum-nickel alloy (Raney nickel) is shown in Fig. 2.5. At least four distinct gray levels are observed, which correspond to three different Al/Ni phases with different Al-Ni compositions (labeled "1," "3," and "4" in Fig. 2.5) and a fourth phase that consists of Al-Fe-Ni (labelled "2"), with the phase containing the highest nickel concentration appearing brightest in the BSE image.

Fig. 2.5 Backscattered electron atomic number contrast for a polished flat surface of Raney nickel (nickel-aluminum) alloy. Numbered locations identify phases with distinctly different compositions

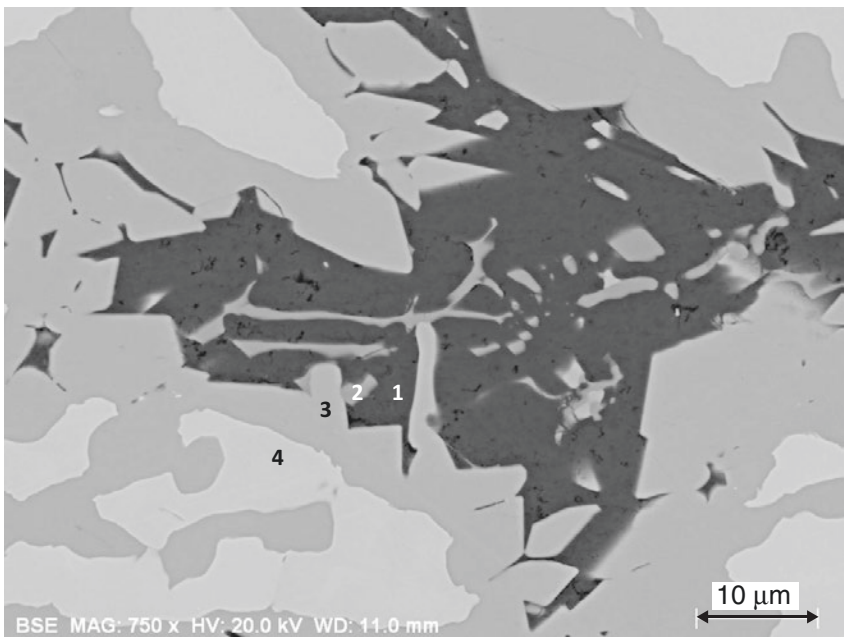

2.2.2 BSE Response to Specimen Inclination (η vs. Surface Tilt, θ)

Model the effect of the angle of inclination of the specimen surface to the incident beam with the Monte Carlo simulation. Select a particular element and incident beam energy, e.g., copper and $E_0 = 20$ keV, and vary the angle of incidence. Calculate at least 10,000 trajectories to obtain adequate simulation precision.

Figure 2.6 shows simulations for aluminum with an incident beam energy of 15 keV at various inclinations calculated with 200 trajectories, which qualitatively reveals the increase in backscattering in a forward direction (i.e., continuing in the general direction of the incident beam) with increasing tilt angle. A more extensive series of simulations for aluminum at $E_0 = 15$ keV with 25,000 trajectories covering a greater range of specimen tilts is presented in Table 2.1, where the backscatter coefficient shows a strong dependence on the surface inclination.

Table 2.1 Backscatter vs. tilt angle for aluminum at $E_0 = 15$ keV (25,000 trajectories calculated with the CASINO Monte Carlo simulation)

Tilt (degrees)	η
0	0.129
15	0.138
30	0.169
45	0.242
60	0.367
75	0.531
80	0.612
85	0.706
88	0.796
89	0.826

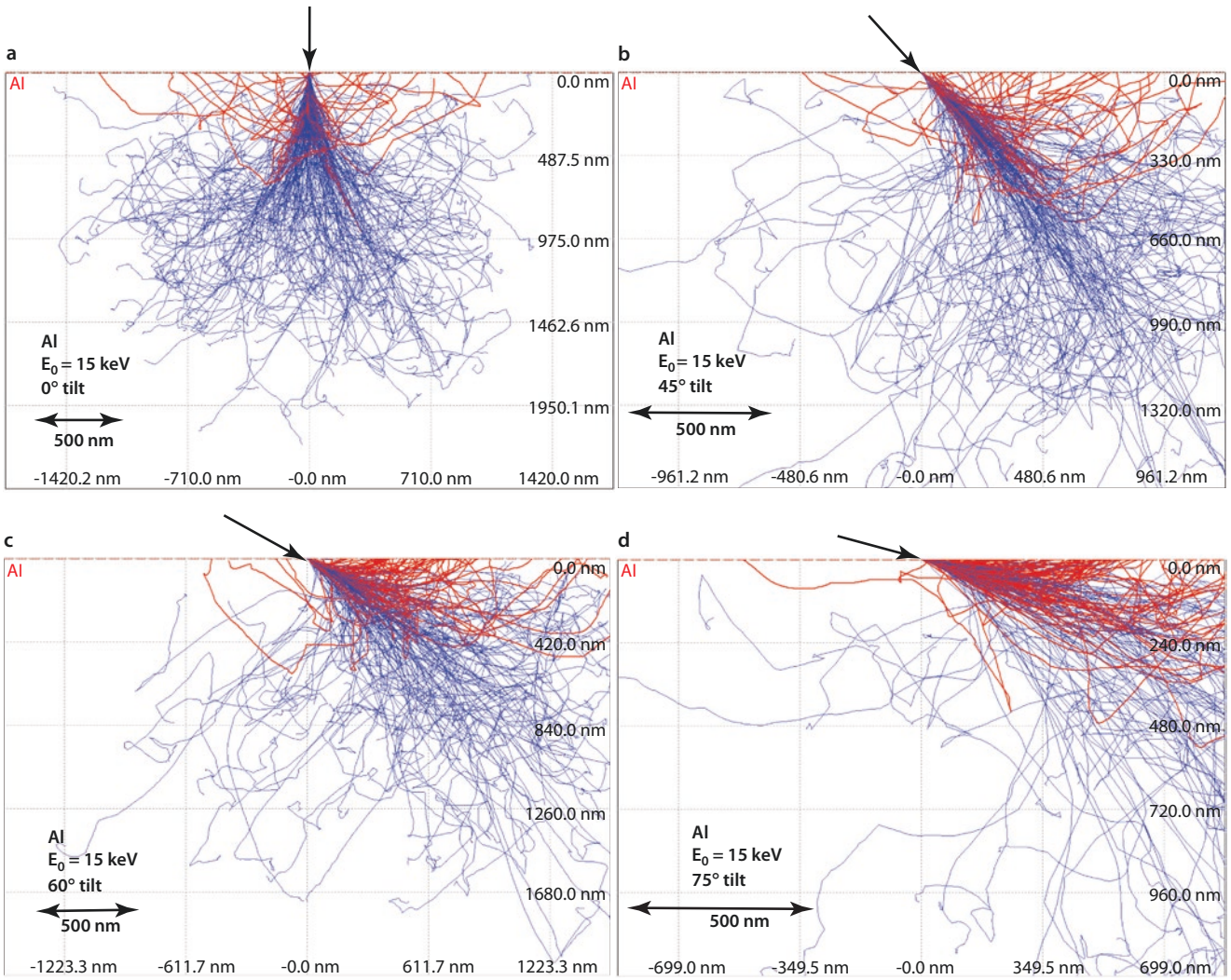

Fig. 2.6 **a** Monte Carlo simulation for aluminum at $E_0 = 15$ keV for a tilt angle of 0°. **b** Monte Carlo simulation for aluminum at $E_0 = 15$ keV for a tilt angle of 45°. **c** Monte Carlo simulation for aluminum at $E_0 = 15$ keV for a tilt angle of 60°. **d** Monte Carlo simulation for aluminum at $E_0 = 15$ keV for a tilt angle of 75°

Figure 2.7 shows the results of similar Monte Carlo simulations for various elements as a function of surface inclination. As the surface tilt increases, η increases for all elements, converging toward unity at high tilt and grazing incidence for the incident beam.

SEM Image Contrast: "BSE Topographic Contrast—Number Effects"

This regular behavior of η vs. θ provides the basis for a contrast mechanism by which differences in the relative numbers of backscattered electrons depend on differences in the local surface inclination, which reveals the surface topography. Figure 2.8a shows an example of a pure material (polycrystalline silver) with grain faces inclined at various angles. The higher the inclination of the local surface to the incident beam, the higher will be the BSE signal, so that highly inclined surfaces appear bright, while dark surfaces are those nearly perpendicular to the beam. This image was prepared with a backscattered electron detector (discussed in the Electron Optics—Detectors module), which has a very large solid angle, so that backscattered electrons are collected with high efficiency regardless of the direction that they travel after leaving the specimen.

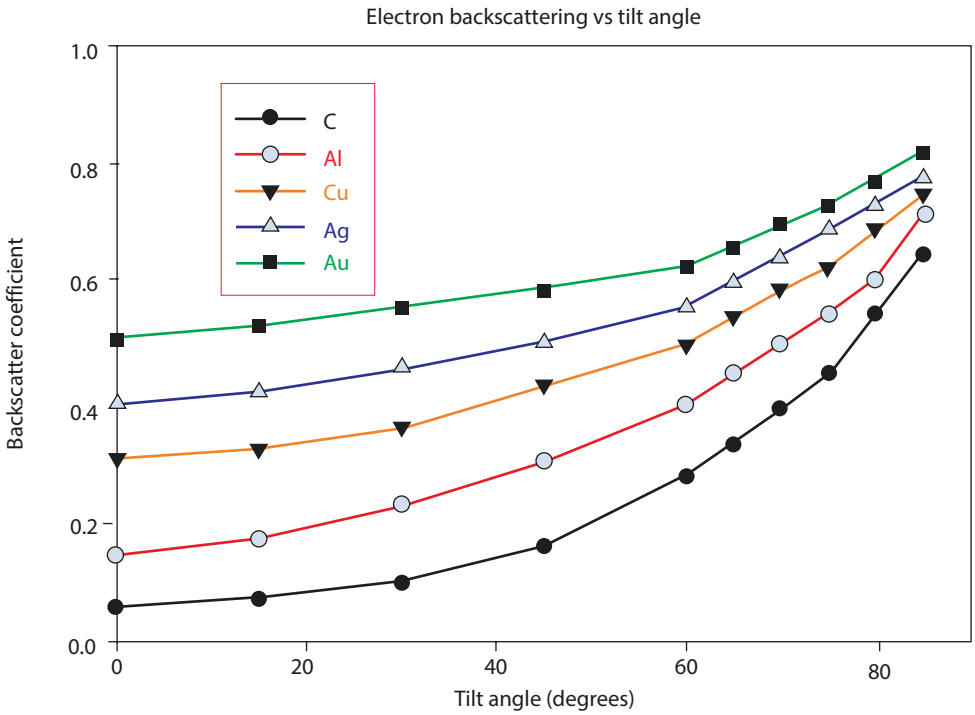

Fig. 2.7 Monte Carlo calculations of electron backscattering from various tilted pure element bulk targets

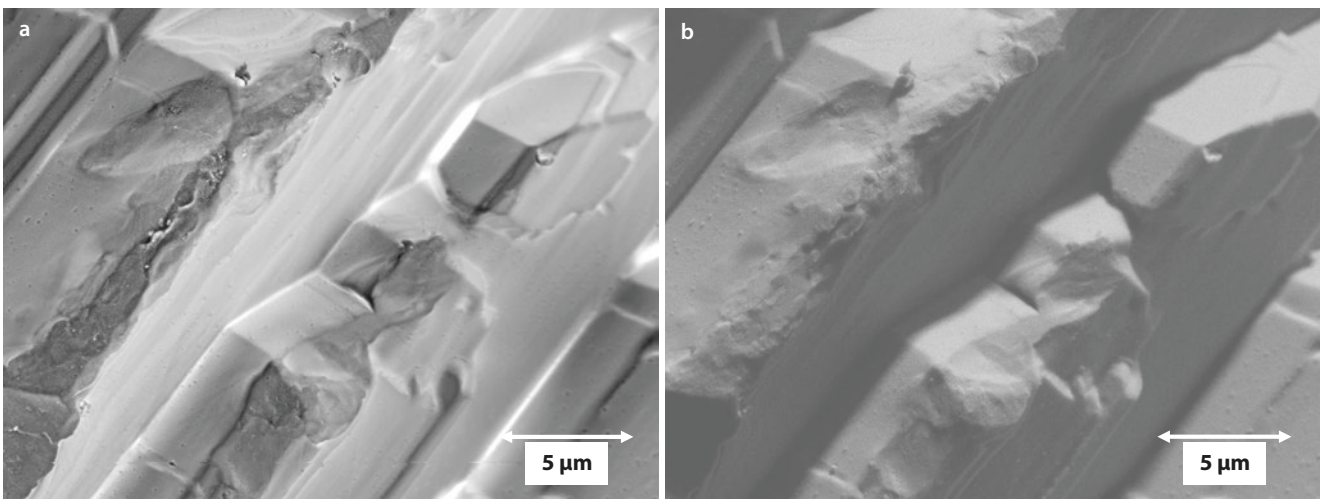

Fig. 2.8 **a** SEM backscattered electron image of a topographically irregular surface of pure silver prepared with a large collection angle BSE detector. **b** SEM backscattered electron image of the same area, prepared with a small collection angle BSE detector placed at the top of the image looking down

2

2.2.3 Angular Distribution of Backscattering

Beam Incident Perpendicular to the Specimen Surface (0° Tilt)

For a flat, bulk target, backscattered electrons emerge through the surface along a wide range of possible angular paths measured relative to the surface normal. When the incident beam is perpendicular to the specimen surface (0° tilt), experimental measurements and Monte Carlo simulations show that the angular distribution of the trajectories is such that the fraction along any given angle of emission is proportional to the cosine of that angle of emission, φ, between the electron trajectory and the surface normal, as shown in Fig. 2.9a:

$$\eta(\varphi) \sim \cos(\varphi) \tag{2.6}$$

Thus, the largest number of BSEs follow a path parallel to the surface normal (φ =0°, cosine = 1), while virtually no BSEs exit along a trajectory nearly parallel to the surface (φ =90°, cosine = 0). The angular distribution seen in Fig. 2.8a is also rotationally symmetric around the beam: the same cosine shape would be found in any section through the distribution in any plane perpendicular to surface containing the beam vector and surface normal.

Beam Incident at an Acute Angle to the Specimen Surface (Specimen Tilt > 0°)

When a flat, bulk target is tilted so that the beam is incident at an acute angle to the surface, the angular distribution of backscattered electrons changes from the rotationally symmetric cosine function of Fig. 2.9a to the asymmetric distribution

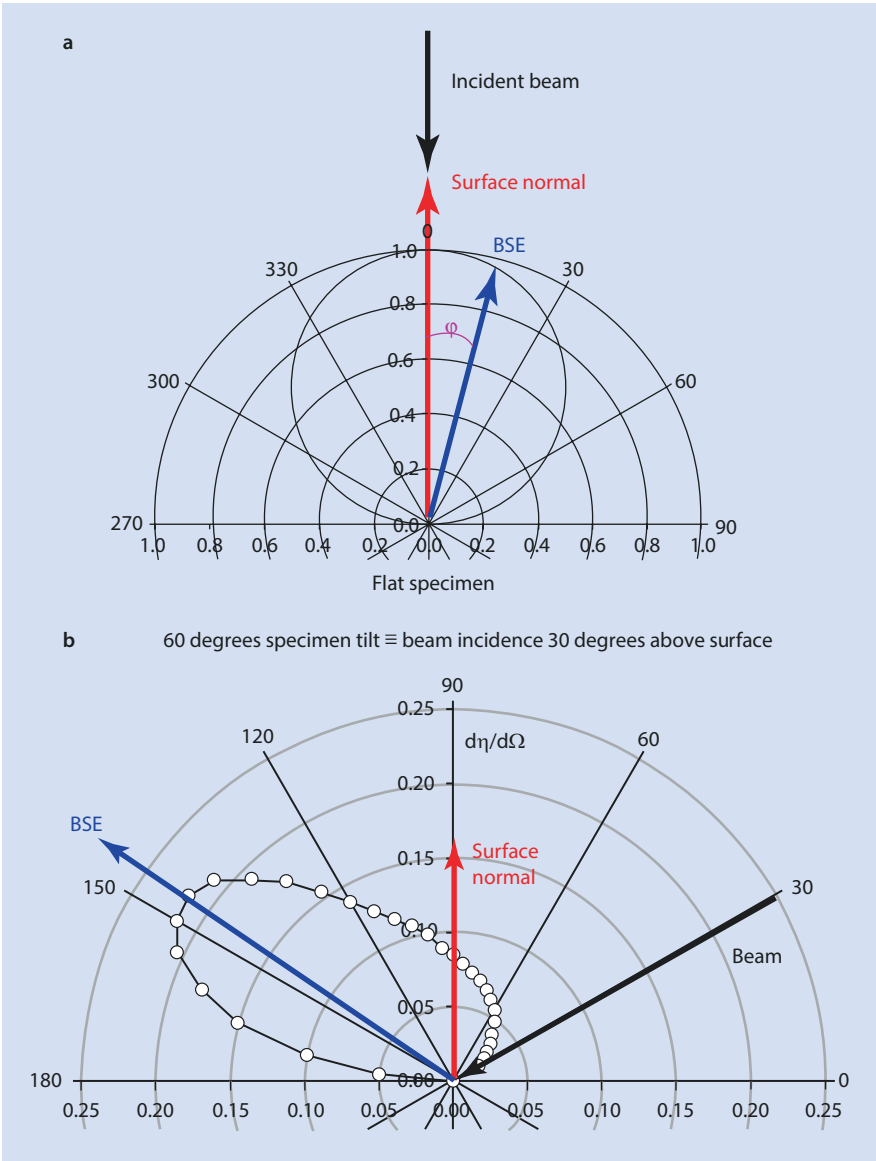

Fig. 2.9 **a** Cosine angular distribution observed for the directionality of backscattering from a bulk target at normal incidence (0° tilt; beam perpendicular to surface). **b** Angular distribution observed for the directionality of backscattering from a bulk target inclined (60° tilt; beam 30° above surface) (Data of Seidel quoted by Niedrig 1978)

seen in Fig. 2.9b, with this distribution measured for a tilt of 60° (angle of incidence = 30°). The angular distribution is peaked in the forward direction away from the incident beam direction, with the maximum BSE emission occurring at an angle above the surface close to the value of the angle of incidence above the surface of the beam. This angular asymmetry develops slowly for tilt angles up to approximately 30°, but the asymmetry becomes increasingly pronounced with further increases in the specimen tilt. Moreover, the rotational symmetry of the 0° tilt case is also progressively lost with increasing tilt, with the asymmetric distribution seen in Fig. 2.9b becoming much narrower in the direction out of the plotting plane. See ▶ Chapter 29 for effects of crystal structure on backscattering angular distribution.

SEM Image Contrast: "BSE Topographic Contrast—Trajectory Effects"

The overall effects of specimen tilt are to increase the number of backscattered electrons and to create directionality in the backscattered electron emission, and both effects become increasingly stronger as the tilt increases. The "trajectory effects" create a very strong component of topographic contrast when viewed with a backscattered electron detector that has limited size and is placed preferentially on one side of the specimen. Figure 2.8b shows the same area as Fig. 2.8a imaged with a small solid angle detector, located at the top center of the image. Very strong contrast is created between faces tilted toward the detector, i.e., facing upward, and those tilted away, i.e., facing downward. These effects will be discussed in detail in the Image Interpretation module.

2.2.4 Spatial Distribution of Backscattering

Model a small number of trajectories (~25) so that the individual trajectories can be distinguished; e.g., for a copper target with an incident beam energy of 20 keV and 0° tilt, as seen in Fig. 2.10 *(Note: because of the random number sampling, repeated simulations will differ from each other and will be different from the printed example.) By following a number of trajectories from the point of incidence to the point of escape through the surface as backscattered electrons, it can be seen that the trajectories of beam electrons that eventually emerge as BSEs typically traverse the specimen both laterally and in depth.*

Depth Distribution of Backscattering

By performing detailed Monte Carlo simulations for many thousands of trajectories and recording for each trajectory the maximum depth of penetration into the specimen before the electron eventually escaped as a BSE, we can determine the contribution to the overall backscatter coefficient as a function of the depth of penetration, as shown for a series of elements in Fig. 2.11a. To compare the different elements, the horizontal axis of the plot is the depth normalized by the Kanaya–Okayama range for each element. From the depth distribution data in Fig. 2.11a, the cumulative backscattering coefficient as a function of depth can be calculated, and as shown in Fig. 2.11b, this distribution follows an S-shaped curve. To capture 90 % of the total backscattering, which corresponds to the region where the slope of the plot is rapidly decreasing, the backscattered electrons are found to travel a

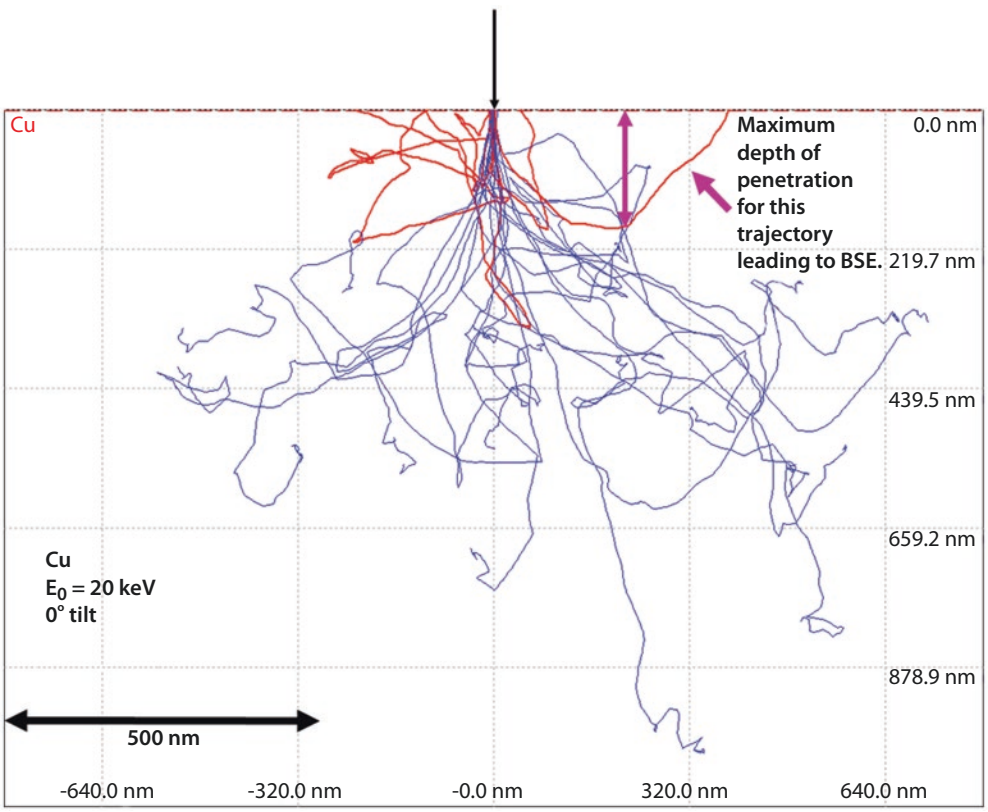

Fig. 2.10 Monte Carlo simulation of a few trajectories in copper with an incident beam energy of 20 keV and 0° tilt to show effect of penetration depth of backscattered electrons

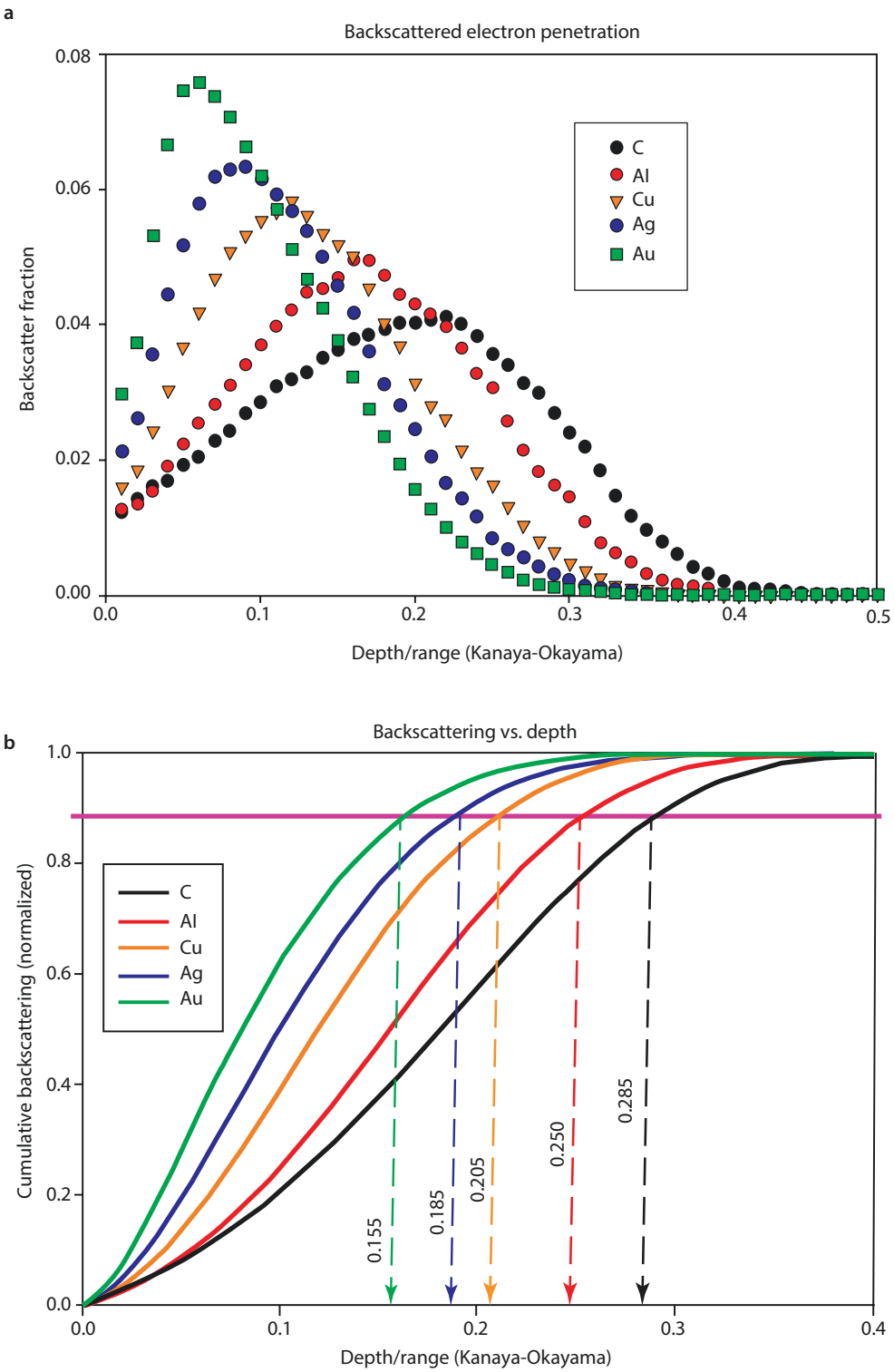

Fig. 2.11 **a** Distribution of depth penetration of backscattered electrons in various elements. **b** Cumulative backscattering coefficient as a function of the depth of penetration in various elements, showing determination of 90 % total backscattering depth

significant fraction of the Kanaya–Okayama range into the target. Strong elastic scattering materials with high atomic number such as gold sample a smaller fraction of the range than the weak elastic scattering materials such as carbon. Table 2.2 lists the fractional range to capture 90 % of backscattering at normal beam incidence (0° tilt) and for a similar Monte Carlo study performed for a target at 45° tilt. For a tilted target, all materials show a slightly smaller fraction of the Kanaya–Okayama range to reach 90 % backscattering compared to the normal incidence case.

When the beam energy is increased for a specific material, the strong dependence of the total range on the incident

Table 2.2 BSE penetration depth ($D/R_{K\text{-}O}$) to capture 90 % of total backscattering

	0° tilt	45° tilt
C	0.285	0.23
Al	0.250	0.21
Cu	0.205	0.19
Ag	0.185	0.17
Au	0.155	0.15

beam energy leads to a strong dependence of the sampling depth of backscattered electrons, as shown in the depth distributions of backscattered electrons for copper over a wide energy range in Fig. 2.12. The substantial sampling depth of backscattered electrons combined with the strong dependence of the electron range on beam energy provides a useful tool for the microscopist. By comparing a series of images of a given area as a function of beam energy, subsurface details can be recognized. An example is shown in Fig. 2.13 for an engineered semiconductor electronic device with three-dimensional layered features, where a systematic increase in the beam energy reveals progressively deeper structures.

Radial Distribution of Backscattered Electrons

The Monte Carlo simulation can record the x-y location at which a backscattered electron exits through the surface plane, and this information can be used to calculate the radial distribution of backscattering relative to the beam impact location. The cumulative radial distribution is shown in Fig. 2.14 for a series of elements, as normalized by the Kanaya–Okayama range for each element, and an S-shaped curve is observed. Table 2.3 gives the fraction of the range necessary to capture 90 % of the total backscattering. The radial distribution is steepest for high atomic number elements, which scatter strongly compared to weakly scattering low atomic number elements. However, even for strongly scattering elements, the backscattered electrons emerge over a significant fraction of the range. This characteristic impacts the spatial resolution that can be obtained with backscattered electron images. An example is shown in Fig. 2.15 for an interface between an aluminum-rich phase and a copper-rich phase ($CuAl_2$) in directionally solidified aluminum-copper eutectic alloy. The interfaces are perpendicular to the surface and are atomically sharp. The backscattered electron signal response as the beam is scanned across the interface is more than an order-of-magnitude broader (~300 nm) due to the lateral spreading of backscattering than would be predicted from the incident beam diameter alone (10 nm).

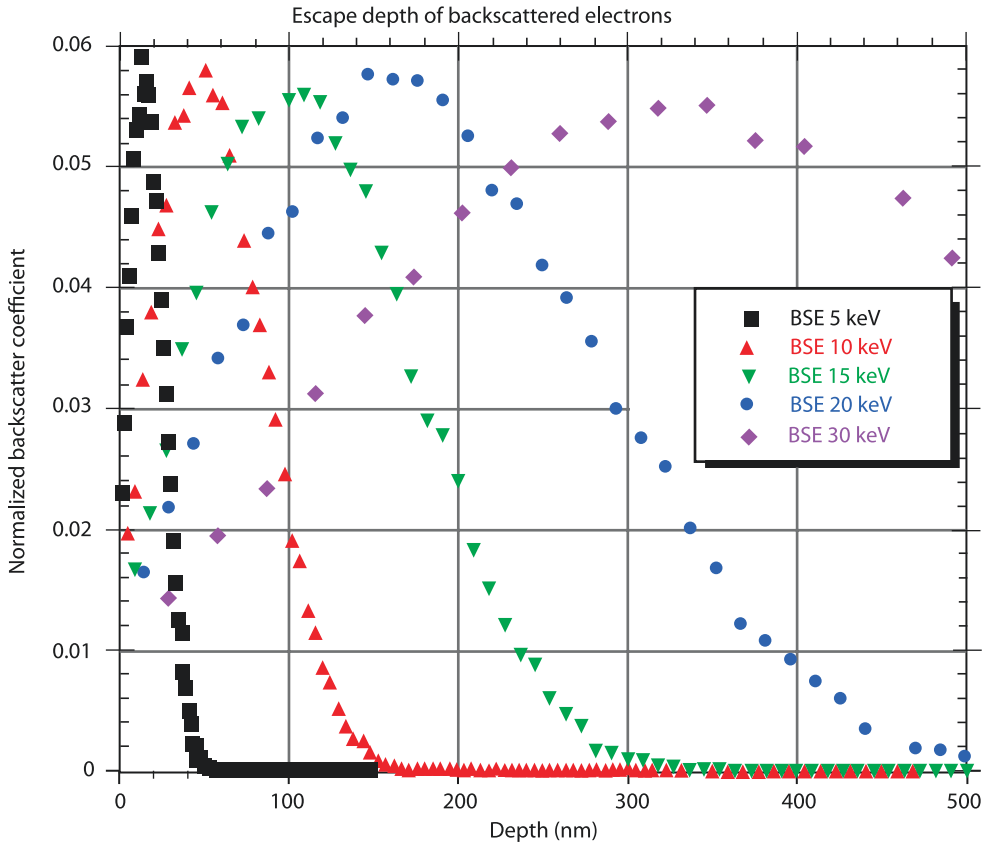

Fig. 2.12 Backscattered electron depth distributions at various energies in copper at 0° tilt

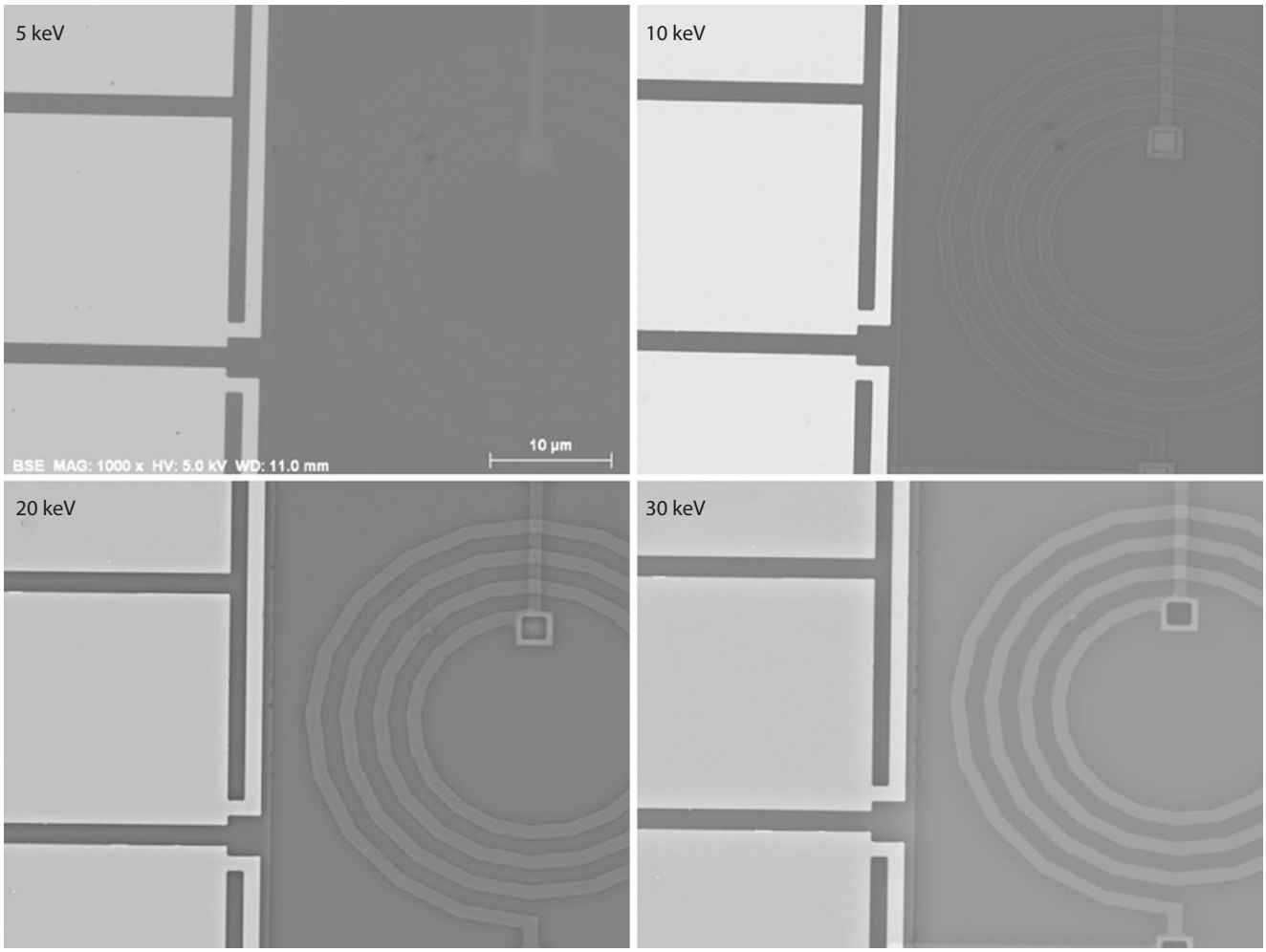

Fig. 2.13 BSE images at various incident beam energies of a semiconductor device consisting of silicon and various metallization layers at different depths

Fig. 2.14 Cumulative radial distribution of backscattered electrons in various bulk pure elements at 0° tilt showing determination of 90 % total backscattering radius

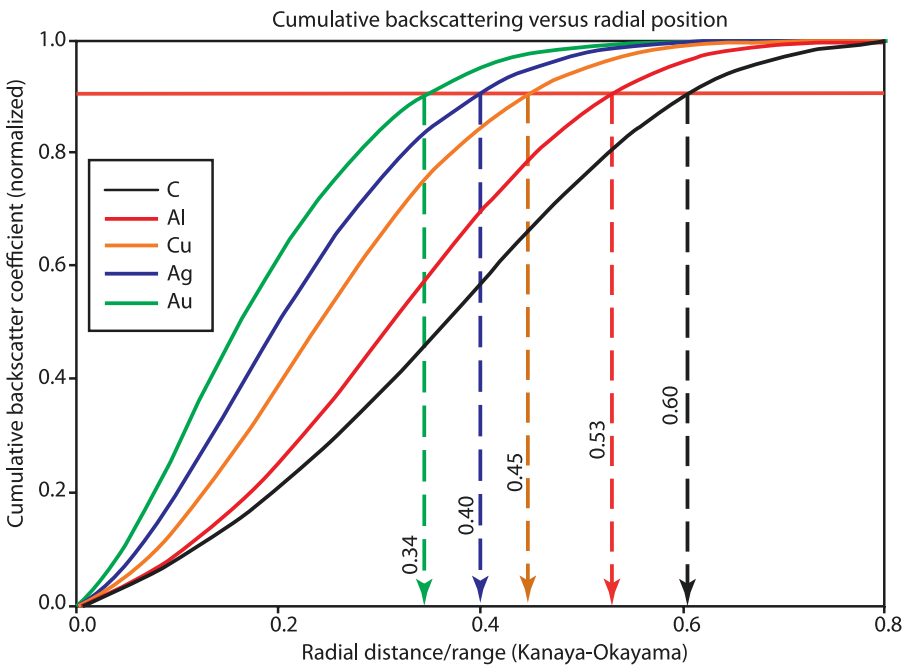

Table 2.3 Fraction of the BSE radial distribution ($r/R_{K\text{-}O}$) to capture 90 % of backscattering

C	0.60
Al	0.53
Cu	0.45
Ag	0.40
Au	0.34

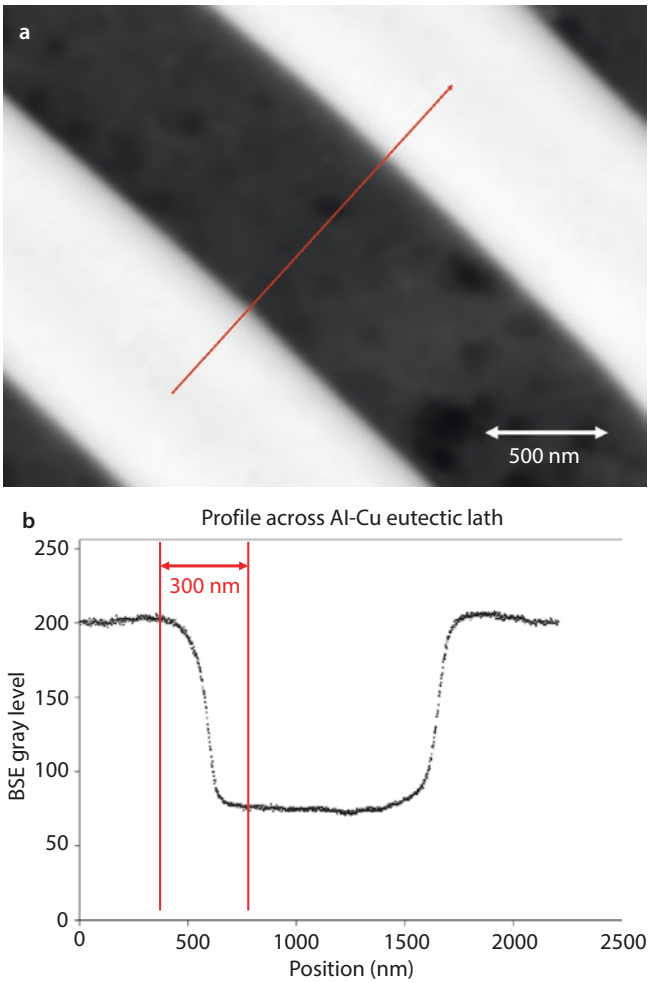

Fig. 2.15 **a** Backscattered electron image of a directionally solidified aluminum-copper eutectic alloy showing two phases: $CuAl_2$ (bright) and an Al-rich solid solution with copper. **b** Trace along the vector indicated in Fig. 2.15a showing BSE signal profile

2.2.5 Energy Distribution of Backscattered Electrons

As a beam electron travels in the specimen, inelastic scattering progressively diminishes the energy. When the trajectory of a beam electron intersects a specimen surface so that backscattering occurs, the backscattered electron will have lost a portion of the initial beam energy, E_0, with the amount lost depending on the length of the path within the specimen. The Monte Carlo simulation can record the exit energy of each backscattered electron, and from this data the energy distribution of BSE can be calculated, as shown in Fig. 2.16a. The energy distribution is seen to extend from the incident beam energy down to zero energy. The energy distribution is sharply peaked at high fractional energy for a strong elastic scattering material such as gold, but the energy distribution is much broader and flatter for a weak elastic scattering material such as carbon. The backscattered electron energy spectra of Fig. 2.16a can be used to calculate the cumulative backscattering distribution as a function of the fractional energy retained, E/E_0, as shown in Fig. 2.16b. It is worth noting that even for weakly scattering carbon, more than half of the backscattered electrons retain at least half of the incident beam energy. The retained energy is a critical property that impacts the design of detectors for backscattered electrons.

2.3 Summary

Backscattered electrons form an important imaging signal for the SEM. A general understanding of the major properties of BSE provides the basis for interpreting images:

1. η vs. Z (atomic number)
2. η vs. θ (specimen tilt)
3. $\eta(\theta)$ vs. φ (emission angle relative to surface normal)
4. η vs. sampling depth
5. η vs. radial distance from beam
6. $\eta(E)$ vs. Z, energy distribution of BSE (Fig. 2.16)

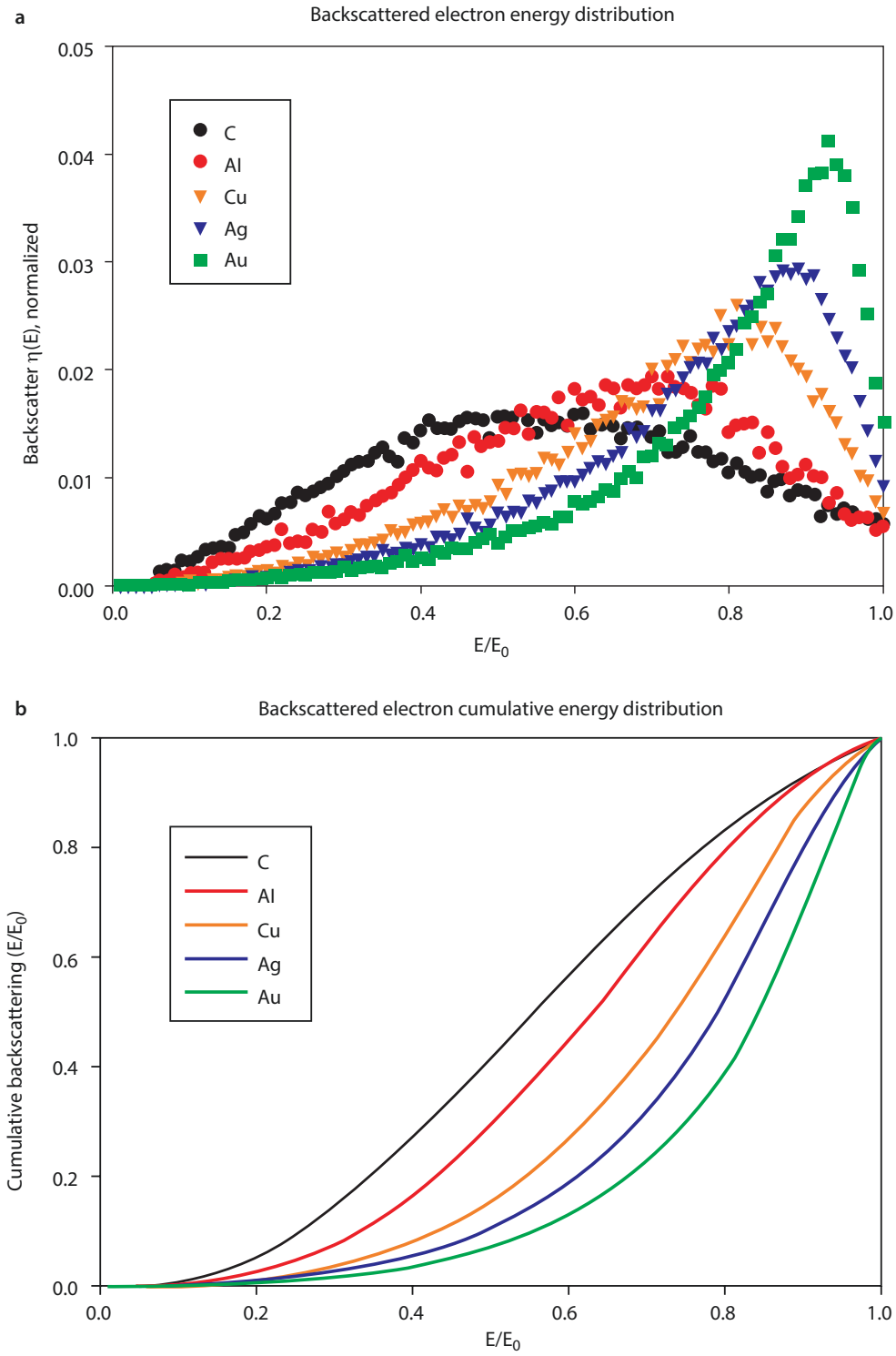

Fig. 2.16 **a** Monte Carlo simulation of the energy of backscattered electrons for various pure elements at $E_0 = 20$ keV and 0° tilt. **b** Cumulative backscattered electron energy distribution for various pure elements at $E_0 = 20$ keV and 0° tilt

References

Bishop H (1966) Some electron backscattering measurements for solid targets. In: Castaing R, Deschamps P, Philibert J (eds) Proceeding 4th international conferences on x-ray optics and microanalysis. Hermann, Paris, p 153

Heinrich KFJ (1966) Electron probe microanalysis by specimen current measurement. In: Castaing R, Deschamps P, Philibert J (eds) Proceeding 4th international conferences on x-ray optics and microanalysis. Hermann, Paris, p 159

Niedrig H (1978) Physical background of electron backscattering. Scanning 1:17

Reuter W (1972) Electron backscattering as a function of atomic number. In: Shinoda G, Kohra K, Ichinokawa T (eds) Proceeding 6th International Cong x-ray optics and microanalysis. University of Tokyo Press, Tokyo, p 121